Ab Initio Computer Simulations on Interfacial Properties of Single-Layer MoS2 and Au Contacts for Two-Dimensional Nanodevices

Gabriele Boschetto, Stefania Carapezzi, Corentin Delacour, Madeleine Abernot, Thierry Gil, Aida Todri-Sanial

Ab Initio Computer Simulations on Interfacial Properties of Single-Layer MoS_2 and Au Contacts for Two-Dimensional Nanodevices

Gabriele Boschetto, Stefania Carapezzi, Corentin Delacour, Madeleine Abernot, Thierry Gil, Aida Todri-Sanial

Laboratory of Computer Science, Robotics, and Microelectronics, University of Montpellier, CNRS, 161 Rue Ada, 34095 Montpellier, France

Email: aida.todri@lirmm.fr

Abstract

The functionality and performance of devices based on atomically thin two-dimensional (2D) materials strongly depends on the quality of the employed 2D material. Although molybdenum disulfide (MoS_2) is an excellent candidate for future applications in nanoelectronics, MoS_2 films have not yet reached the level of purity achieved in silicon technologies. At present, the formation of small and extended defects in the material is inevitable during the growth process, and this has a non-negligible impact on the electronic properties of MoS_2. Furthermore, defects are also thought to affect non trivially the resistance at the MoS_2-metal contact and the injection of carriers. In this work, we systematically and thoroughly assess the impact of some of the most commonly occurring defects in MoS_2 (such as vacancies, substitutions, and grain boundaries) not only from the point of view of the material's properties but also by looking at MoS_2-metal contacts. To do so, we carry out ab initio computer simulations in the density functional theory (DFT) framework coupled with surface simulations based on the Green's function formalism. Our simulation approach allows us to obtain more realistic models of MoS_2 interfaces with Au. Moreover, this is the first theoretical study in which the effect of grain boundaries on the MoS_2-Au contact properties is explored. Results suggest S vacancies to have a detrimental effect on the quality of the metal contacts, whereas Mo vacancies strongly improve the electron injection from the metal to MoS_2. Antisite Mo defects also lead to an increased electron injection rate by acting as "conductive bridges" between the Au electrode and the 2D material. Finally, each of the grain boundaries here considered improves the quality of the contact. We expect our study to provide the necessary theoretical foundation for the design of MoS_2-metal contacts with suitable characteristics.

1 Introduction

Atomically thin two-dimensional transition metal dichalcogenides (TMDs) have attracted a great deal of interest for future applications in nanoelectronics.[1–5] In particular, monolayer molybdenum disulfide (MoS_2) has been shown to display highly desirable mechanical, electronic, and optical properties due to its intrinsic reduced dimensionality, which could also enable very compact and low-power devices. For instance, MoS_2 has a very good carrier mobility at room temperature (estimated to be as high as $\sim 400\ cm^2\,V^{-1}\,s^{-1}$),[6,7] and chemical stability up to 1100 °C. Moreover, in contrast with graphene, monolayer MoS_2 shows a direct sizeable band gap of 1.8 eV,[8] thus making such material suitable for a wide range of devices including field-effect transistors (FETs), memory devices, and optoelectronics.[9–13]

Pivotal for the use of MoS_2 in electronic devices is the possibility of wafer-scale production, which nowadays is mostly achieved via chemical and/or physical vapor deposition (CVD and PVD, respectively). However, while both techniques could be suitable for mass production, the resulting material is often far from being pristine. Structural defects such as vacancies, substitutions, and grain boundaries are introduced in MoS_2, and these have been shown to significantly affect the material's properties.[14–19] For instance, transistors built with CVD- and PVD-grown single-layer MoS_2 have shown significantly lower carrier mobilities (45 $cm^2\,V^{-1}\,s^{-1}$ and $>1\ cm^2\,V^{-1}\,s^{-1}$, respectively) with respect to the ideal value cited above.[20] This has been argued to be due to the high concentration of defects (typically on the order of $10^{13}\,cm^{-2}$) in the material's surface.[21] However, such defects may also have a positive impact on the overall functionality of nanodevices: for instance, one of the proposed working mechanisms of 2D memristors made of monolayer MoS_2 involves the migration of point defects (mainly sulfur mono-vacancies) with the formation of conductive-like channels. This would result in the modulation of the material's resistance at the interface with the metal electrode, and would explain the capability of the device to switch from its high-resistance state (HRS) to its low-resistance state (LRS).[11,22,23] Sun et al. demonstrated how defects can also enhance the adsorption of Li on monolayer MoS_2, therefore improving the energy storage capabilities of such material in the context of Li-ion batteries.[24] Grain boundaries have

also been shown to be crucial for the functionality of MoS_2-based memristors: Xu and co-authors[25] built a device made of bi-layer MoS_2, and they demonstrated that its working mechanism is due to the migration of metallic ions from the Cu electrode to MoS_2, which is facilitated by the presence of grain boundaries in the material. In addition, it was shown that grain boundaries play a crucial role for the functionality of the memristor devices built by Sangwan and co-authors.[26]

Overall, there is clear evidence of the non-negligible impact of structural defects on the electronic properties of monolayer MoS_2, and in turn on the performance and on the working mechanisms of 2D nanodevices. Moreover, equally important is the choice of the metal electrode: for instance, some metals can chemically react with MoS_2, whereas others are only weakly interacting with the material via weak dispersion forces. Clearly, this has a strong impact on the contact resistance at the metal-MoS_2 junction.[27–29] Furthermore, Fermi level pinning at the MoS_2-metal contact could also lead to large Schottky barriers and contact resistances, which are known to limit the device performance by introducing unwanted parasitic elements.[30,31] Indeed, one of the drawbacks of TMDs is the generally higher metal-semiconductor contact resistivity with respect to other 2D materials, such as graphene.[32] Among the many different options, Au is perhaps one of the most commonly used elements to build electrodes in MoS_2-based devices, due to its stability and chemical inertness. Moreover, Au can also act as the support when growing large-area monolayer MoS_2.[33]

Clearly, a deep understanding of the physics and chemistry at the interface between Au and MoS_2 would be highly beneficial, in order to elucidate the interface energetics, carrier injection rates, and more generally to improve the design of metal contacts in 2D nanodevices. To this end, theoretical simulations based on atomistic approaches are undoubtedly useful, as in real samples different defects might be present in the material simultaneously. Thus, simulations allow us to i) assess and predict the impact of defects on the properties of both the 2D material and the interface, and ii) disentangle the effect of different defects. Indeed, the ideal defect-free Au-MoS_2 interface has been already widely studied.[27–29] However, as previously mentioned, experimentally-grown MoS_2 often presents a high number of structural defects. More recently, theoretical studies on the interaction between Au and defective MoS_2 have also been carried out: for instance, Tumino et al. combined STM images and large density functional theory (DFT) simulations to elucidate the role of point defects in single-layer MoS_2 supported on Au(111).[34] Yang et al. studied the impact of sulfur vacancies in tuning the n- and p-type characteristics of MoS_2 in top contact with Au electrode.[35] Qiu and co-authors also carried out DFT simulations of defective MoS_2-Au interfaces, mainly focusing on the role and concentration of sulfur mono-vacancies on the charge redistribution at the contact interface.[36]

However, we point out that such studies focused on a limited subset of point defects, mainly sulfur vacancies and small clusters. Moreover, to the best of our knowledge, no studies have been carried out yet considering MoS_2 structures with grain boundaries in contact with Au. Therefore, in this work we perform accurate atomistic DFT simulations of defective Au-MoS_2 interfaces consisting of a larger set of structural defects commonly occurring with both CVD and PVD growth methods,[14] with also the inclusion of grain boundaries. Additionally, in our simulations we employ surface models based on the Green's function approach, in order to have a more realistic representation of the metal electrodes rather than carrying out simulations based on slab models. To the best of our knowledge, this is the first time that such a simulation approach has been used to study defective Au-MoS_2 interfaces.

This work consists of two parts: first, as the essential prerequisite to the following more complex simulations, we investigate the properties of point defects and grain boundaries (GBs) in free-standing MoS_2, i.e., without the inclusion of the metal electrode. This allows us to assess the impact of defects on MoS_2 itself, and to validate our simulation approach. Then, the knowledge gained in the first part of this study is used as a starting point to carry out the main part of this work, which consists on the investigation of the chemistry and physics at the Au-MoS_2 interface. In summary, we want to thoroughly understand the properties of Au-MoS_2 contacts in realistic conditions, i.e., with a defective 2D material.

This paper is organized as follows: in the following section (Simulations Details) we describe the setup of our computer simulations and the model employed; in Results and Discussion we discuss on our simulations of defective MoS_2 and Au-MoS_2 interfaces, in the context of 2D devices. Finally, Conclusions are presented in the final section.

2 Simulation Details

In this work, we considered monolayer MoS_2 with either point defects or grain boundaries, in top contact with the Au electrode. Given the high number of structural defects experimentally observed in such material, we only focused on those which are the most abundant with both CVD and PVD growth techniques, as discussed by Hong et al. in their work.[14] The point defects here considered are: sulfur mono-vacancy (V_S), sulfur di-vacancy (V_{S2}), molybdenum vacancy (V_{Mo}), antisite Mo filling one S mono-vacancy (Mo_S), antisite Mo filling one S di-vacancy (Mo_{S2}), and two Mo atoms filling one S di-vacancy ($Mo2_{S2}$). These are all shown in Figure 2. Interestingly, the first three types of defects mostly occur with the CVD method, whereas the latter three with PVD. Regarding the grain boundaries, we have considered three representative cases characterized by a tilt angle of 60°: two mirror-symmetric GBs (4|4P and 4|4E), and one asymmetric GB (8|4). The 4|4P structure consists of a series of 4-fold rings connected by a shared point, whereas in 4|4E the 4-fold rings all share an edge; finally, the structure of 8|4 consists of alternating 4- and 8-fold rings. The structure of these GBs are shown in Figure 4. We point out that both 4|4P and 4|4E have been frequently observed in experimentally-grown MoS_2 samples,[16,37–40] with the former being among the most commonly occuring GBs in MoS_2,[41]. Also, 8|4 has already been discussed in the literature.[37,42–44]

We first studied the electronic properties of free-standing MoS_2 with either point defects or GBs. To study isolated structures

Table 1: Simulation cell parameters of Au-MoS_2 interfaces with the inclusion of GBs.

Parameter	Au-4|4E	Au-4|4P	Au-8|4
a (Å)	45.9004	53.9631	53.2194
b (Å)	3.19013	3.16922	5.54199
c (Å)	49.3090	47.6598	49.3582
α	90.0000°	90.0000°	90.0000°
β	90.0000°	90.0000°	90.0000°
γ	93.3374°	100.116°	65.3823°

with point defects, we considered 5×5 hexagonal MoS_2 supercells to obtain realistic defect concentrations, within the experimental range of $\sim 10^{13}$ cm^{-2}. We ensured an in-plane distance between the structure of GBs of at least 15 Å to avoid any spurious interaction. Likewise, we also included at least 20 Å of vacuum below and above the MoS_2 layer, in the out-of-plane direction.

We then coupled each of these structures with the Au(111) top electrode. We ensured that the induced strain due to the lattice mismatch between the mono-layer and the metal was as small as possible, compatibly with the feasibility of the simulations. We point out that since it is well known that the electronic properties of MoS_2 can be significantly affected by strain,[45] only the structure of the Au electrode was strained. We note that the calculated in-plane lattice constant of MoS_2 was 3.16 Å, in very good agreement with experimental data.[46] When considering point defects, we started from a 3×3 orthorombic MoS_2 supercell, and we positioned Au(111) on top, thus obtaining an orthorombic Au-MoS_2 interface simulation cell. The resulting mean absolute strain on Au was low and ∼3%. By choosing such a MoS_2 supercell we were able to maintain once again the concentration of defects within the typical range of values found in experiments ($\sim 10^{13}$ cm^{-2}). The simulation cell parameters of each Au-MoS_2 interface were a= 16.4219 Å, b= 9.4812 Å, c= 45.5679 Å, and α= 90°, β= 90°, γ= 90°. From this point onward, we will refer to the defect-free interface as Au-MoS_2, whereas if point defects are considered we will write Au- followed by the abbreviation of the defect. For instance, Au-V_S refers to the interface between Au and MoS_2 with the inclusion of one S mono-vacancy.

We followed the same strategy when constructing interfaces between Au and MoS_2 with GBs, in order to minimize as much as possible the artificial strain on Au while striving to maintain the number of atoms as low as possible. Similarly with point defects, we will refer to the structures with GBs as Au- followed by the abbreviation of the GB. We obtained interfaces with an induced mean absolute strain on Au of ∼4% in both Au-4|4E and Au-4|4P, and of ∼2% on Au-8|4. We point out that the interface structures here constructed were not necessarily orthorombic, and the simulation cell parameters are shown in Table 1.

Atomistic simulations were carried out in the framework of density functional theory (DFT) with QuantumATK atomic-scale modelling software.[47,48] We performed spin-polarized calculations in vacuum using the Perdew-Burke-Ernzerhof (PBE) exchange-correlation functional,[49] and to model core electrons we used norm-conserving pseudopotentials from the PseudoDojo library.[50] We employed the LCAO approach with a density-mesh

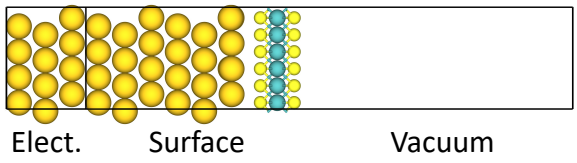

Figure 1: Schematics of the Green's function surface model used in this work to simulate Au-MoS_2 interfaces. The structure here shown is the optimized interface at the PBE-D2 level between Au and pristine MoS_2. On the left side, the fully periodic bulk Au electrode is shown, whereas on the left side the surface-vacuum interface can be seen.

cut-off of 200 Ry for the isolated point defects and GBs, and of 150 Ry for the interface models. The QuantumATK-optimized Medium basis set was used throughout this work. When modelling interfaces we also included the Grimme's D2 dispersion correction[51] to take into account dispersion interactions. Geometry optimizations of free-standing defective MoS_2 were carried out with a convergence threshold of the atomic forces of 0.01 eV/Å, and in all simulatons we employed a **k**-point mesh defined by a $5 \times 5 \times 1$ Monkhorst-Pack (MP) grid,[52] whereas for computing the density of states (DOS) we employed a $9 \times 9 \times 1$ MP grid.

To model Au-MoS_2 interfaces we carried out Green's function surface calculations as implemented in QuantumATK:[53] in contrast to the widely used slab method, surface calculations within the Green's function formalism allow us to construct Au surfaces which are essentially fully periodic in one direction, and therefore with only one single surface-vacuum interface. In addition to obtaining models which are more physically realistic, simulations are also significantly less affected by the size of the surface thickness. We constructed our surface models by considering MoS_2 coupled with six atomic Au layers. We imposed Neumann boundary conditions in the vacuum direction and Dirichlet boundary conditions at the boundary with the bulk Au electrode (see Figure 1). Given the size and the computational cost associated with such systems, simulations of point defects were carried out with a $2 \times 3 \times 138$ MP grid, whereas to compute device density of states we used an MP grid defined by a $8 \times 12 \times 138$ **k**-point mesh. Geometry optimizations were converged with a maximum allowed atomic force threshold of 0.05 eV/Å. For the interfacial GBs we used the following settings: $1 \times 12 \times 138$ for Au-4|4P, $1 \times 12 \times 138$ for Au-4|4E, and $1 \times 7 \times 128$ for Au-8|4.

3 Results and Discussion

3.1 Electronic Properties of Defective MoS_2

The first part of this study, which serves as a prerequisite for further simulations on Au-MoS_2 interfaces, is dedicated to the analysis of the structure and the electronic properties of MoS_2 with the inclusion of either small point defects or extended defects (grain boundaries). As discussed in the previous sections, it is well known that MoS_2 grown by common methods like CVD and PVD is far from being a pristine material, as numerous defects are

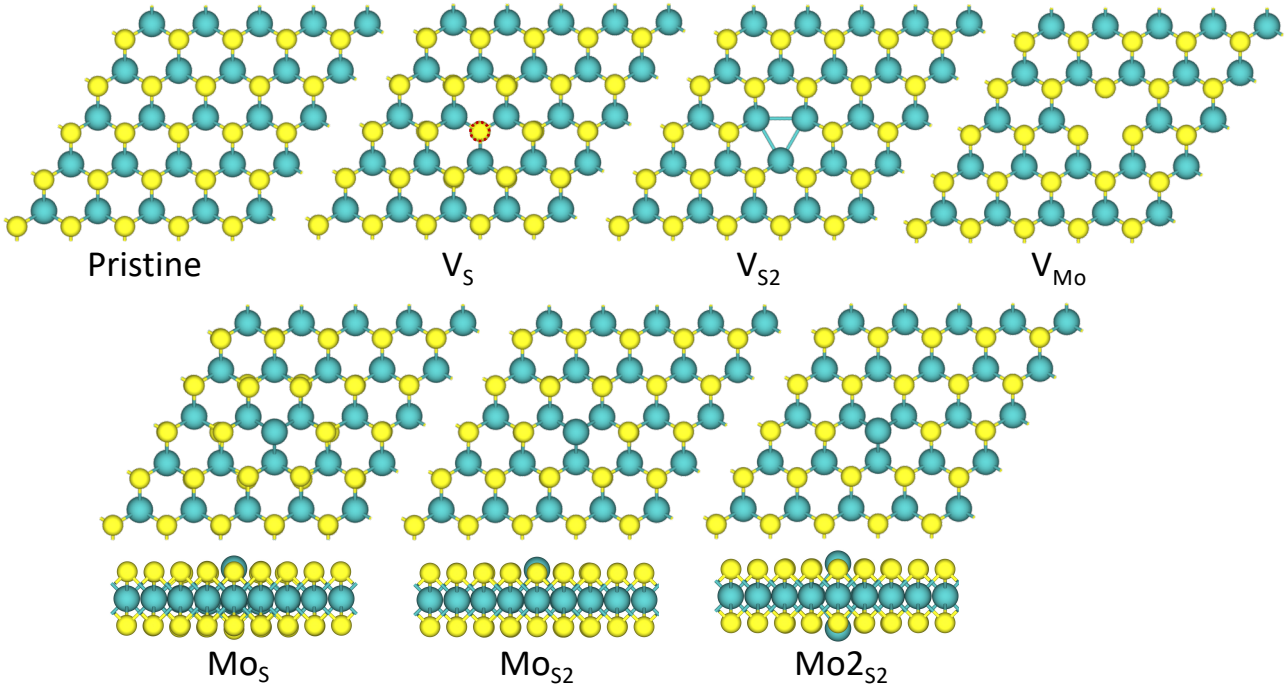

Figure 2: Optimized structures at the PBE level of the 5×5 hexagonal supercells of pristine and defective MoS_2. Starting from the top left and following the pristine material, V_S stands for sulfur mono-vacancy, V_{S2} for sulfur di-vacancy, and V_{Mo} for molybdenum vacancy. Those in the bottom are all antisite Mo defects, where Mo_S represents the antisite Mo atom filling one S mono-vacancy, Mo_{S2} the same antisite atom filling one S di-vacancy, and $Mo2_{S2}$ two Mo antisite atoms filling one S di-vacancy. For each antisite Mo defect the side view of the optimized structure is also shown for clarity.

inevitably introduced following the growth and annealing procedures. Point defects can reach high concentrations, typically on the order of $\sim 10^{13}$ cm^{-2}. It is clear that with such high defect densities the electronic properties of the material could be dramatically different from the ideal defect-free case.

From the structural point of view, we found that introducing point defects (either vacancies or substitutions) leads to a small atomic rearrangement of the MoS_2 structure, as can be observed in Figure 2, where the DFT-optimized geometries of pristine and defective MoS_2 are shown. V_{S2} caused the three surrounding Mo atoms to move closer in order to fill the gap left by the two axial S atoms. We observed the Mo-Mo distance of such three atoms to significantly decrease from 3.17 Å to 2.85 Å. On the contrary, with V_{Mo} the three surrounding S atoms moved slightly away from the gap left by the missing Mo atom, thus reducing the Mo-S bond length from 2.42 Å to 2.38Å. In each Mo antisite defect the extra Mo atom occupies the position of the missing S atom, thus forming bonds with the three surrounding Mo atoms in the core of MoS_2. The bond length between the extra substitutional Mo and the three core Mo atoms was found to be 2.58 Å, which is larger than the typical Mo-S bond length (2.42 Å). Indeed, from Figure 2 it can be observed that the antisite Mo atom sticks out slightly of the basal plane of MoS_2. Finally, we also note that when two antisite Mo atoms are present ($Mo2_{S2}$) they are found to lie on the same vertical axis. Overall, given the size of the MoS_2 supercell which ensures a reasonable defect concentration of $\sim 4.6\times10^{13}$ cm^{-2}, we found point defects to have a limited and rather localized effect on the MoS_2 crystal structure.

To investigate the impact of point defects on the electronic properties of MoS_2 we computed the density of states (DOS) of both the pristine and the defective material (see Figure 3), with projections onto the relevant atomic orbitals of S and Mo (S-3p and Mo-4d). As can be seen from the figure, our simulations predicted pristine MoS_2 to be a seminconductor with a band gap of 1.79 eV, in excellent agreement with the experimental value of $\sim$1.8 eV.[8] Moreover, as expected the S-3p and Mo-4d orbitals are those with the most significant contribution to the overall DOS. Then, we found that S vacancies (V_S, V_{S2}) introduced localized intra-gap states, whose contribution is significantly given by the Mo-4d orbitals with respect to S-3p orbitals. These extra states are located above the Fermi level and $\sim$0.57 eV from the edge of the material's conduction band. We note that this is consistent with previous DFT simulations.[12,18] We point out that in their work Bhattacharjee et al.[12] found the extra states to be located $\sim$0.73 eV from the edge of the conduction band, however the authors used a much larger supercell (8×8) to simulate defective MoS_2. This effectively reduces the concentration of the S vacancies with respect to our study. We expect this to have a non-negligible effect on the energy of the intra-gap states, although our simulations essentially predict the same. In addition, in V_{S2} we observed additional states overlapping with the material's conduction band edge. Then, we found that V_{Mo} led to a number of deep intra-gap states, some located below the Fermi level, and others above the Fermi level. Interestingly, we observed that the states below the Fermi level and closer to the valence band edge of MoS_2 are given almost exclusively by the S-3p

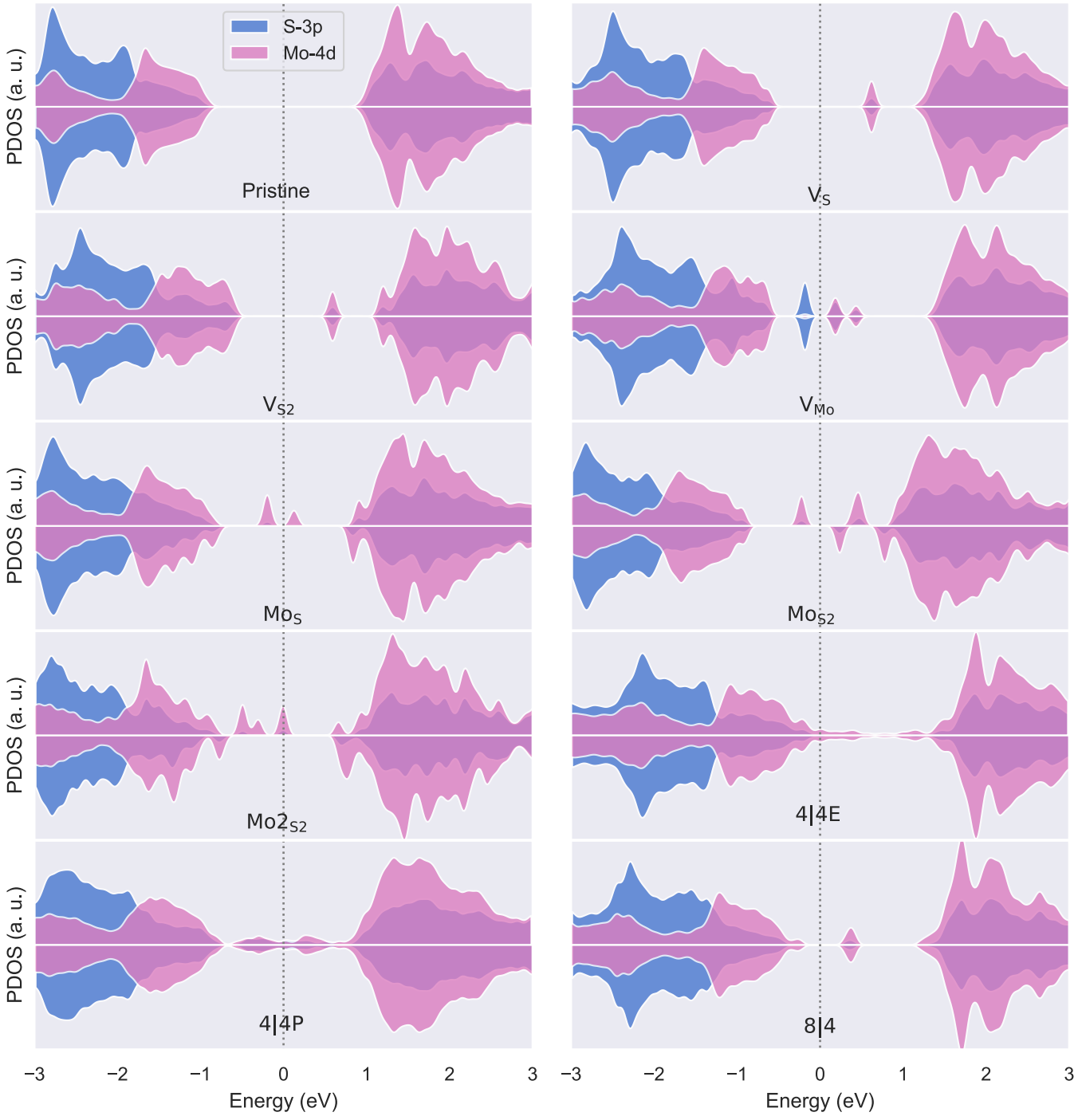

Figure 3: Projected density of states (PDOS) of pristine and defective MoS_2 with the inclusion of small point defects and grain boundaries. The projections are onto the relevant atomic orbitals of Mo and S. The plots are centered around the Fermi level of each system, and the curves were obtained with a Gaussian smearing of 0.05 eV.

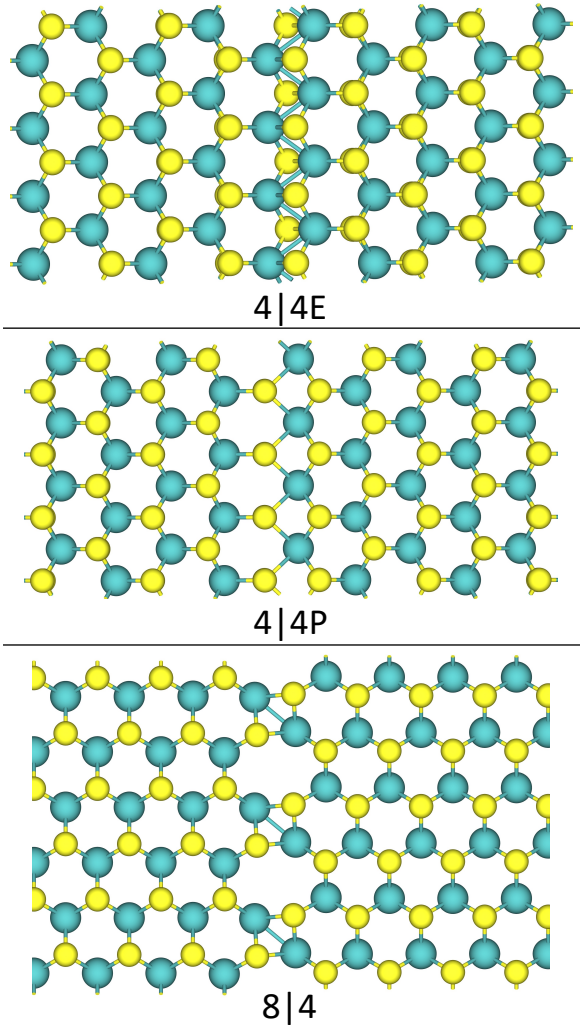

Figure 4: Optimized structures at the PBE level of the grain boundaries (GBs) in MoS_2 considered in this work.

orbitals, whereas in the states above the Fermi level both S-3p and Mo-4d show a significant contribution. From the projected DOS (PDOS) shown in Figure 3 one can also observe that vacancies do no induce any magnetic moment in the material. On the contrary, antisite Mo substitutions were all found to induce a spin magnetic moment of 1.8 μ_B, 2.0 μ_B, and 4.0 μ_B in Mo_S, Mo_{S2}, and $Mo2_{S2}$, respectively. Previous theoretical studies[14,54] on Mo_S and Mo_{S2} antisite defects also corroborate our present findings. The presence of a non-zero magnetic moment in Mo antisite defects was explained as the result of two extra unpaired electrons on antisite Mo coming from the surrounding Mo atoms. Similarly to vacancies, each of these antisite defects was found to introduce a number of intra-gap states in MoS_2, whose contribution to the overall DOS is given almost exclusively by the 4d orbitals of the Mo atoms.

Following the study on point defects, we then focused on the electronic properties of grain boundaries. The optimized structures are shown in Figure 4, whereas the PDOS of the GBs are shown in Figure 3, once again projected onto the 3p and 4d orbitals of S and Mo, respectively. From the same figure it is possible to observe that both 4|4E and 4|4P introduced a significant number of low intra-gap states in the material, effectively leading to the vanishing of the band gap. This corroborates previous studies claiming that such GBs may lead to 1D metallic strips in MoS_2.[41,55] Differently from 4|4E and 4|4P, 8|4 only led to the appearance of localized deep intra-gap states, above the Fermi level. The orbital contribution on the intra-gap states in GBs is given mainly by Mo-4d orbitals, with a smaller contribution by S-3p. Finally, we also note that none of the GBs here considered showed any spin magnetic moment.

In conclusion, we found that both point and extended defects have a significant impact on the electronic and magnetic properties of MoS_2: the appearance of either localized or diffused intra-gap states is expected to dramatically modify the material's transport properties. This in turn could have a significant impact on the performance of electronic devices based on MoS_2. However, so far only the isolated material has been considered. In a device, the 2D material will be in contact with a metal electrode. Thus, in the next part we will focus on defective MoS_2 in contact with the Au metal electrode.

3.2 Structure and Properties of Au-MoS_2 Interfaces

3.2.1 Geometry of Interfaces

In this second and main part of our work, we focused on the structural and electronic properties of MoS_2 in contact with the Au electrode. At first, to gain a qualitative insight into the physics and chemistry at the Au-MoS_2 interface, we investigated the structure of both materials once in contact, and we calculated the average interface distance (d_{Au-MoS_2}) of each structure, as defined in Figure 5. Additionally, we computed the electron density difference (EDD) maps of the interfaces to visualize the redistribution of charge upon creating the contact between the two materials. EDD maps can also be used to qualitatively assess the strength of the interaction between Au and MoS_2 and the overlap between orbitals. EDD maps are shown in Figure 6.

Initially, we focused on defect-free Au-MoS_2 (see Figure 1 for the optimized geometry of the system), and we found an average interface distance of 2.71 Å, in very good agreement with previous values reported in the literature.[27,34,56] We note that the relatively large value of d_{Au-MoS_2} effectively limits the orbital overlap between Au and MoS_2, and prevents any chemical bonding to occur. Indeed, our results are once again consistent with the literature: the formation of a van der Waals (vdW) gap between Au and MoS_2 was reported, as well as the interface to be characterized by weak dispersion forces. Such a weak interaction can be explained by the d-band model, as Au has fully occupied d bands.[57] Finally, we did not observe any significant structural rearrangement of the atoms of either Au or MoS_2, confirming the weak interaction between the two materials. These findings correlate with the EDD map of the defect-free interface in Figure 6, which shows a very limited charge redistribution mainly at the surface of MoS_2.

We then looked at defective Au-MoS_2 interfaces in the presence of small point defects. The DFT-optimized structures of

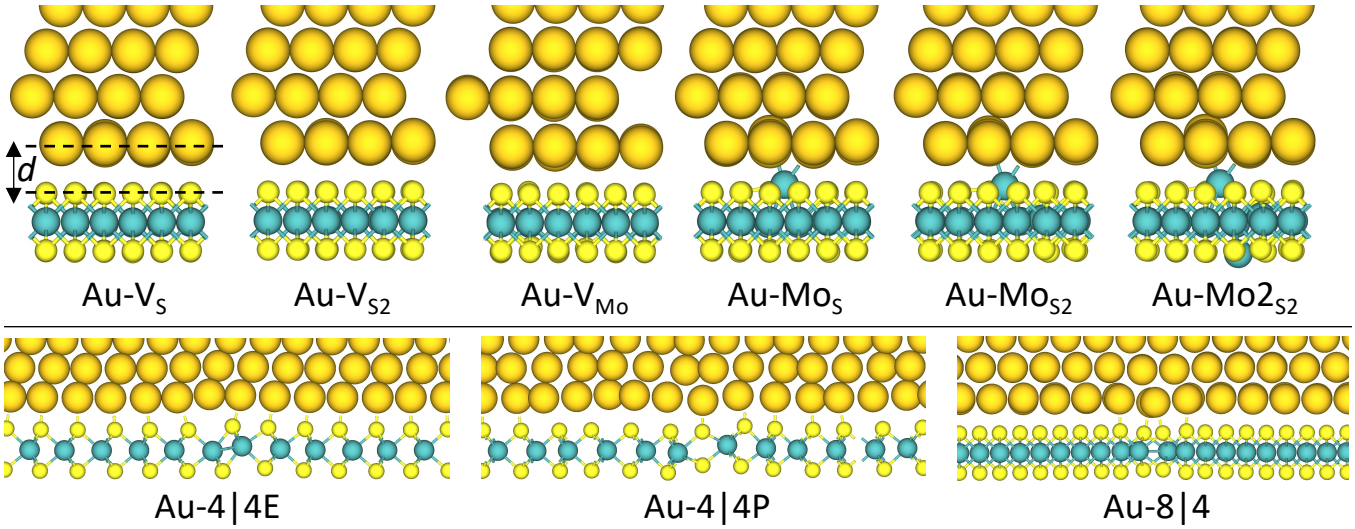

Figure 5: Optimized structures at the PBE-D2 level of the Au-MoS_2 interfaces with the inclusion of point defects (top) and grain boundaries (bottom). For clarity, the structures are shown in the proximity of the interface between the two materials. The parameter d is defined as the average interface separation distance.

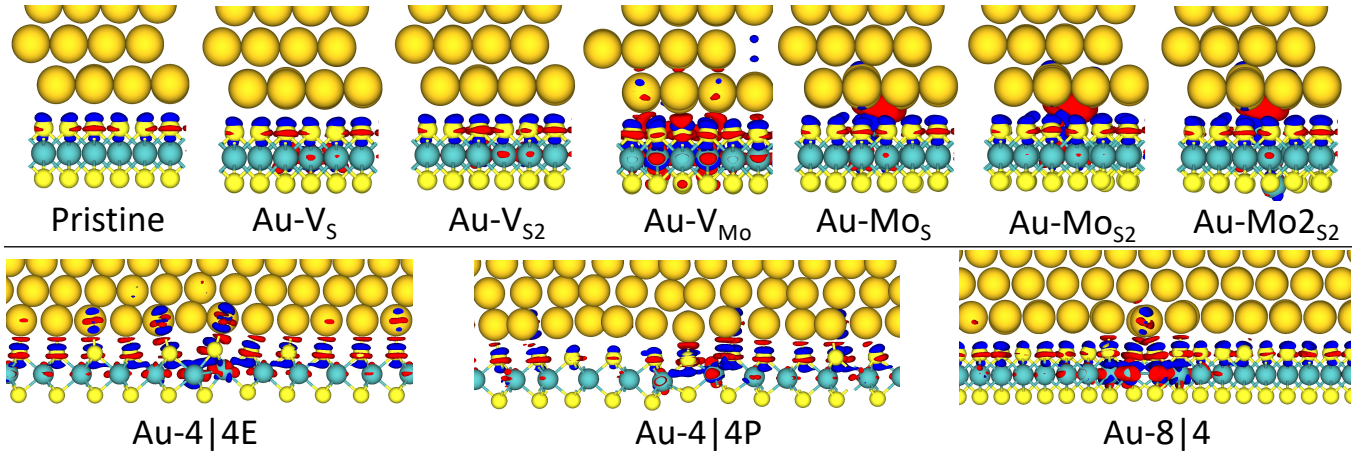

Figure 6: Electron density difference (EDD) maps of the Au-MoS_2 interfaces considered in the present study. Point defects are shown at the top, whereas GBs at the bottom. The red isosurface refers to electron enrichment, whereas the blue isosurface to electron loss. Isovalue is 0.002 eV/Å^3.

such systems are shown in Figure 5. As can be seen from the figure, we found that introducing small point defects in MoS_2 caused, to some extent, the displacement of the atoms at the interface between the two materials. With both V_S and V_{S2} such a displacement was limited, and involved mainly the atoms at the bottom-most layer of Au. Similarly, the change in d_{Au-MoS_2} was not appreciable, its value being 2.73 Å and 2.70 Å in Au-V_S and Au-V_{S2}, respectively. We note that the EDD maps of both structures essentially confirm the limited effect of such vacancies, as qualitatively such EDD maps do not significantly differ from that of the defect-free material. Interestingly, in the Au-V_{Mo} interface we observed a significant variation of the crystal structure of the Au contact, presumably caused by the reactivity of the three S atoms in proximity of the Mo vacancy. Due to the lack of Mo, such S atoms change from a 3-fold coordination (typical of the defect-free material) to a 2-fold coordination, which explains the enhanced reactivity towards the Au surface. Indeed, although on average d_{Au-MoS_2} did not vary with respect to the defect-free case, we observed the displacement of three Au atoms, which moved closer to the 2-fold S atoms with distances between 2.53 Å and 2.59 Å. The stronger orbital coupling between Au and V_{Mo} can also be seen in Figure 6, where the charge redistribution is significant. The EDD is not limited to the interface region only but extends further into the second Au layer and throughout MoS_2.

Regarding the interfaces with antisite Mo defects, we observed a significant displacement of both the atoms at the bottom-most Au layer and the extra Mo atom in the MoS_2 surface. As discussed in the previous section, and as can be seen from both Figure 2 and Figure 5, the substitutional Mo atoms filling the S vacancies do not lie on the same plane as the other S atoms. The bond length with the core Mo atoms of MoS_2 is longer than the typical Mo-S bond length. We predicted the average vertical separation between the antisite Mo atoms and the Au layer to be as short as 2.28 Å, 2.36 Å, and 2.22 Å in Au-Mo_S, Au-Mo_{S2}, and Au-$Mo2_{S2}$, respectively. Furthermore, the presence of the Au interface caused the displacement of antisite Mo atoms towards the bridge site between two Au atoms from the metal contact. In each of the Au-Mo_S, Au-Mo_{S2}, and Au-$Mo2_{S2}$ systems we found the bond length between Mo and the two Au atoms to be 2.75-2.79 Å, a range of values comparable with the Au-Au bond length in the Au lattice (2.75 Å). This suggests a strong reactivity of Mo towards the Au surface, and most likely an enhanced orbital coupling between Au and MoS_2. This is confirmed by looking at the EDD maps of these systems, where a significant charge redistribution around the extra Mo antisite atom occurs. Furthermore, we computed the electron localization function (ELF) of these systems, and we could confirm the formation of a chemical bond between the extra antisite Mo atom and the two Au atoms from the metal electrode. The ELF plot of the representative Au-MoS system is shown in Figure S4 in the Supporting Information.

Finally, given the widely experimentally reported abundance of V_S in the material and the importance of such a defect on the functionality of 2D devices such as memristors, we additionally assessed the impact of V_S concentration on the interface properties of Au-MoS_2 contacts. We point out that, by using the simulation cell described in the Simulation Details section, the initial defect concentration with one single S vacancy per unit cell was 6.4×10^{13} cm^{-2}. By randomly introducing a second and a fourth S vacancy we achieved a higher defect concentration of 1.3×10^{14} cm^{-2} and 2.6×10^{14} cm^{-2}, respectively. Similarly to the case of a single S vacancy, we observed a small rearrangement of the Au atoms at the interface with MoS_2, and a limited effect on the average value of d_{Au-MoS_2}, which decreased from 2.71 Å to 2.67 Å (see Figure S1 in the Supporting Information). We expect such a decrease in d_{Au-MoS_2} to have a limited impact on the orbital overlap between the two materials. This is corroborated by the EDD maps of both systems shown in Figure S2 (see Supporting Information). We note that this finding is in contrast with the work of Yang et al.[35] who performed similar studies on defective Au-MoS_2 interfaces and found that increasing the concentration of S vacancies led to the collapse of some Au atoms from the Au electrode to fill the S vacancies in MoS_2. We could assume this to be an artifact of the simulation approach employed in their work, which involved a slab model of the Au interface rather than the more realistic Green's function surface model here used. Another reason could be that in their work the authors created a cluster of four S vacancies, whereas in our work we randomly introduced the S vacancies to avoid any artificial clustering or pattern.

When considering interfaces with GBs, shown in Figure 5, we observed a non-negligible decrease of the average interface distance not only with respect to the defect-free material but also to the material with point defects. Indeed, we found d_{Au-MoS_2} = 2.43 Å, 2.50 Å, 2.63 Å in Au-4|4E, Au-4|4P, and Au-8|4, respectively. Interestingly, by looking at the DFT-optimized structures we observed a significant decrease of d_{Au-MoS_2} in proximity of the grain boundary in both Au-4|4P and Au-8|4. Indeed, from Figure 5 it can be observed that the displacement of the Au atoms is significant above the GBs in MoS_2. On the contrary, we found a more intimate contact (and thus an expected stronger orbital overlap) in Au-4|4E, where the interaction between MoS_2 and the Au electrode extends over the whole interface rather than being localized around the GB. This explains the shorter value of d_{Au-MoS_2} with respect to the other two GBs here considered. The EDD maps of such systems in Figure 6 confirmed our findings: indeed, it is possible to observe a significant charge redistribution in the proximity of the 8|4 and 4|4P grain boundaries, whereas the charge redistribution in Au-4|4E is essentially delocalized over the entire MoS_2 surface.

3.2.2 Tunnelling Barriers

Tunnelling barriers and tunnelling probabilities are useful parameters that can be used to estimate the electron injection rate (and thus the charge transport) through the Au-MoS_2 contact. The tunnelling barrier is a consequence of the absence of covalent bonds between the 2D material and the Au electrode. A high probability of electron tunnelling suggests a strong orbital overlap between the two materials, and therefore a reduced contact resistance is expected. To extract such quantities, we computed the average effective potential (V_{eff}) of each interface structure, and we projected it along the direction of the Au-MoS_2 contact. By considering the shape of the potential barrier as a rectangle, the tunnelling

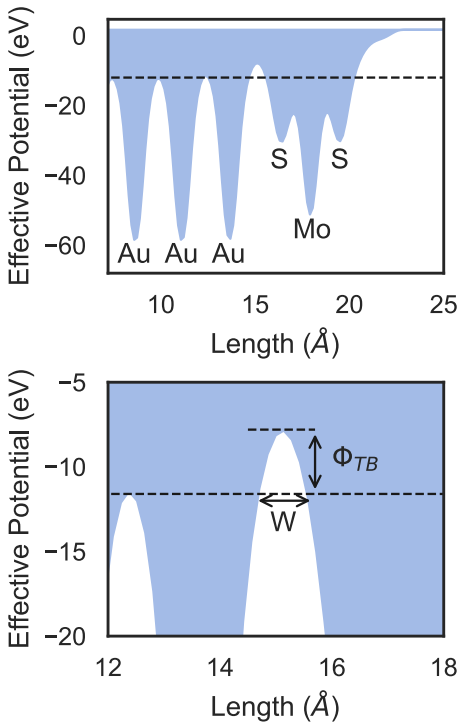

Figure 7: Average effective potential of the defect-free Au-MoS_2 structure, projected along the direction of the interface (top). The bottom plot shows the zoomed area at the interface region. Φ_{TB} is the vertical tunnelling barrier, whereas W is the barrier width.

probability (T) can then be defined as follows:[58]

$$T = e^{-2\left(\sqrt{\frac{2m}{\hbar^2}\Phi_{TB}}\right)W}, \quad (1)$$

where m is the electron mass, $\hbar$ is the reduced Planck's constant, Φ_{TB} is the vertical tunnelling barrier, and W is the width of such barrier. As an example, Figure 7 shows the average effective potential of the defect-free Au-MoS_2 interface, in the proximity of the contact area. As can be seen from the figure, we calculated Φ_{TB} as the difference between the minimum effective potential of Au and the value of the effective potential at the interface gap.[27] A summary of the computed parameters for each Au-MoS_2 interface is shown in Table 2.

We first considered the defect-free interface, and we found a rather large tunnelling barrier (Φ_{TB} = 3.54 eV), corroborating the contact between Au and MoS_2 to be weak and the orbital overlap limited. Interestingly, we note that experimental estimates of the Schottky barrier height (SBH) of Au-MoS_2 contacts range between 0.13-0.32 eV in MoS_2-based FETs[59,60] and 0.48±0.12 eV in MoS_2 exfoliated on template-stripped Au.[61] Moreover, theoretical simulations predicted this value to be higher but still within 1 eV.[30,58] There appears to be a lot of variability in terms of SBH, which could be due to different experimental settings, a different quality of MoS_2, and different device architectures. Nevertheless, we predicted Φ_{TB} to be more than 3 times larger than the SBH obtained via simulations and also significantly larger with respect to the experimental values. This suggests Φ_{TB} to have a very large

Table 2: Summary of the interface parameters of Au-MoS_2 contacts computed in this work. d_{Au-MoS_2} is the average interface distance, Φ_{TB} is the vertical tunnelling barrier, and T is the tunnelling probability. In the three antisite Mo defect structures, the average vertical separation between the extra Mo atom and the Au bottom layer is also shown in parentheses.

Structure	d_{Au-MoS_2} (Å)	Φ_{TB} (eV)	T (%)
Pristine	2.71	3.54	19.4
Au-V_S	2.73	3.55	18.5
Au-V_{S2}	2.70	3.64	18.3
Au-V_{Mo}	2.71	1.04	64.1
Au-Mo_S	2.71 (2.28)	2.87	27.4
Au-Mo_{S2}	2.71 (2.36)	3.07	24.9
Au-$Mo2_{S2}$	2.71 (2.22)	2.77	29.4
Au-4|4P	2.50	3.19	24.8
Au-4|4E	2.43	3.02	27.3
Au-8|4	2.63	3.23	23.6

contribution towards the contact resistance at the Au-MoS_2 interface, and therefore to possibly be one of the main limiting factors in the device performance. Indeed, the large tunnelling barrier resulted in a low tunnelling probabilty of 19.4%, suggesting a rather poor electron injection from the metal to the semiconductor, and therefore a high contact resistance. We point out that both values compare very well with those obtained by Wang et al. (Φ_{TB} = 3.51 eV, T = 15.27%), who performed similar theoretical studies on unstrained and strained defect-free MoS_2-metal interfaces.[58] However, in real devices to have a perfect MoS_2 sheet is very unlikely. Hence, it becomes extremely important to assess the effect of defects on tunnelling barriers and probabilities.

We then considered interfaces with the defective material, and we found that introducing sulfur mono- and di-vacancies in MoS_2 led to a slight increase of Φ_{TB}, thus suggesting the worsening of the contact. Indeed, the tunnelling probability decreased to 18.5% and 18.3% in Au-V_S and Au-V_{S2}, respectively. As previously discussed, we also increased the concentration of V_S and we observed T to further decrease to 18.0% with four S vacancies. Overall, these results suggest that S vacancies have a detrimental effect on the quality of the Au-MoS_2 contact and on the electron injection rate. On the contrary, we observed the opposite effect when introducing one Mo vacancy: Φ_{TB} decreased by a factor of 3 with respect to the pristine material (1.04 eV against 3.54 eV) and, as a consequence, T dramatically increased to 64.1% suggesting a significant decrease of the contact resistance. This correlates with the large atomic displacement observed at the interface discussed in the previous section due to the dangling bonds of the three S atoms surrounding the Mo vacancy. Antisite Mo defects also led to an overall decrease of the vertical tunnelling barrier, and to the increase of the tunnelling probability: we found T= 27.4%, 24.9%, and 29.4% in Au-Mo_S, Au-Mo_{S2}, and Au-$Mo2_{S2}$, respectively. Such an increased electron injection rate may be explained by looking at the extra Mo atom, which acts as a "connecting bridge" between the Au electrode and MoS_2, thus facilitating the electron transfer between the two materials and also lowering the contact resistance. As previ-

ously mentioned, this is confirmed by the ELF plot in Figure S4.

Overall, our results suggest that the presence of either di- or S mono-vacancies worsens the quality of the contact between Au and MoS_2, whereas antisite Mo defects appear to bring a non-negligible improvement. It is worth noting that vacancies (S and Mo) are generated mainly via CVD method, whereas antisite Mo defects via PVD. This means that the choice of the MoS_2 growth method is crucial, and needs to be considered extremely carefully when fabricating devices. For instance, from the point of view of the contact resistance only, PVD samples would probably be a good choice to improve the electron injection rate from the Au electrode to the 2D material. A reduced contact resistance would be undoubtedly beneficial for devices like FETs, in order to limit parasitic currents and to lower the power consumption. On the contrary, in devices like 2D memristors based on single-layer MoS_2, where a high-resistance state (HRS) is needed, PVD samples would probably hinder the whole device functionality, and thus we could argue that CVD-MoS_2 would be a much better choice. Mo vacancies also appear to exceptionally improve the contact between Au and MoS_2, although we point out that in real samples the concentration of such a defect is orders of magnitude lower than that of S mono-vacancies. Thus, we expect the simulations carried out in this work to overestimate the impact of V_{Mo} on the interface properties. Nevertheless, if Mo vacancies are desired these could also be introduced in the material via surface engineering, for instance by heavy ion irradiation[62] or by chemical treatment.[63]

Then, we focused on GBs and we observed that these also led to an overall non-negligible increase in the tunnelling probability (see Table 2): we found T= 27.3%, 24.8%, and 23.6% in Au-4|4E, Au-4|4P, and Au-8|4, respectively. This is once again consistent with the results discussed in the previous section: in general, the higher values of T with respect to the defect-free material correlate with the decrease of the average interface separation distance caused by the GBs, which led to the formation of some chemical bonds at the Au-MoS_2 interface. Moreover, the high tunnelling probability observed in Au-4|4E can be explained by the extended interaction between Au and MoS_2, as previously discussed.

Overall, our results suggest that the unusual bonding of S and Mo at the boundary leads to an increased reactivity of MoS_2 towards the metal electrode. Therefore, in the context of 2D devices GBs may lead to extended areas with a locally-reduced contact resistance. GBs are inevitably formed during the material growth, and thus it is pivotal to be able to control the crystallinity of MoS_2 in order to control, in turn, the concentration and the type of GBs. As our results showed that GBs improve the electron injection, it may be beneficial to engineer such extended defects in order to increase their concentration, which could reach very high values up to 10^{12} cm^{-2}.[64] This could be achieved, for instance, with annealing, mechanical strain, and irradiation.[65,66]

3.2.3 Electronic Properties

Finally, we looked at the DOS of the interface structures, projected onto the 4d orbitals of the core Mo atoms of MoS_2, as shown in Figure 8. By looking at the PDOS of the defect-free Au-MoS_2 interface it is possible to observe that the band gap of the 2D material is mostly retained, suggesting a very limited band hybridization between MoS_2 and the 5d orbitals of Au. Once again, as previously discussed, this is consistent with the formation of a weak vdW gap between Au and MoS_2, and with the low electron injection rate. Additionally, we note a significant shift of the Fermi level towards the conduction band edge of MoS_2, suggesting the n-type doping of the 2D material, consistently with both experiments and previous theoretical findings.[27,36,67] Sulfur mono- and di-vacancies added a number of additional intra-gap states above the Fermi level of the system, as could also be seen in the free-standing material (see Figure 3). However, as the interaction between the two materials is still weak, we note that the band gap of MoS_2 is essentially retained, and its metallization limited. We found similar results when increasing the concentration of S vacancies, as can be seen in Figure S3 in the Supporting Information. Interestingly, in Au-V_{Mo} it is possible to observe a high number of interfacial gap states, extending from the conduction band into the original material's band gap. Moreover, we note that these states cross the Fermi level of the system, suggesting a strong band hybridization and the metallization of MoS_2. This further corroborates our previous findings on the very strong interaction between the metal contact and the 2D material with Mo vacancies. It should be noted, as previously mentioned, that the concentration of V_{Mo} would be much lower in real samples, and therefore the impact of such a defect is most likely to be more limited.

On average, with Mo antisite defects we could observe a more significant metallization of MoS_2 with respect to both Au-V_S and Au-V_{S2}. For each of the structures (Au-Mo_S, Au-Mo_{S2}, Au-$Mo2_{S2}$) the presence of interfacial gap states induced by the Au electrode is evident. We assume this effect to be due to the presence of the extra antisite Mo atom on the MoS_2 surface: as discussed in the previous sections, such Mo atom is able to bridge the Au electrode with the 2D material, effectively facilitating the orbital overlap and increasing the electron injection rate (see Table 2). On a final note, we observed a negligible spin magnetic moment in Au-Mo_S and Au-Mo_{S2}, differently from the free-stading material (see also Figure 3). Moreover, Au-$Mo2_{S2}$ showed a significant decrease of the spin magnetic moment from 4.0 μ_B (in the free-standing material) to 0.7 μ_B. This effect could be explained by the dislocation of the extra Mo atom upon contacting MoS_2 with the Au electrode. Such a dislocation leads to the loss of one Mo-Mo bond, thus removing the magnetism. Therefore, the magnetic moment in Au-$Mo2_{S2}$ derives from the second antisite Mo atom which dislocated from its original position only partially.

Among the interfaces with GBs, Au-4|4E is the structure that shows the most significant metallization, and this is the case also when compared with the systems in the presence of point defects. We could argue this to be the consequence of the extended interaction of 4|4E with the metal electrode, as our previous results suggested (see EDD maps in Figure 6). We observed a significant band hybridization between Au and MoS_2 also in Au-4|4P and Au-8|4, although somewhat less evident than in the previous case. On a final note, as we did not observe any significant spin magnetic moment in Au-4|4P, we assume the peak in the PDOS

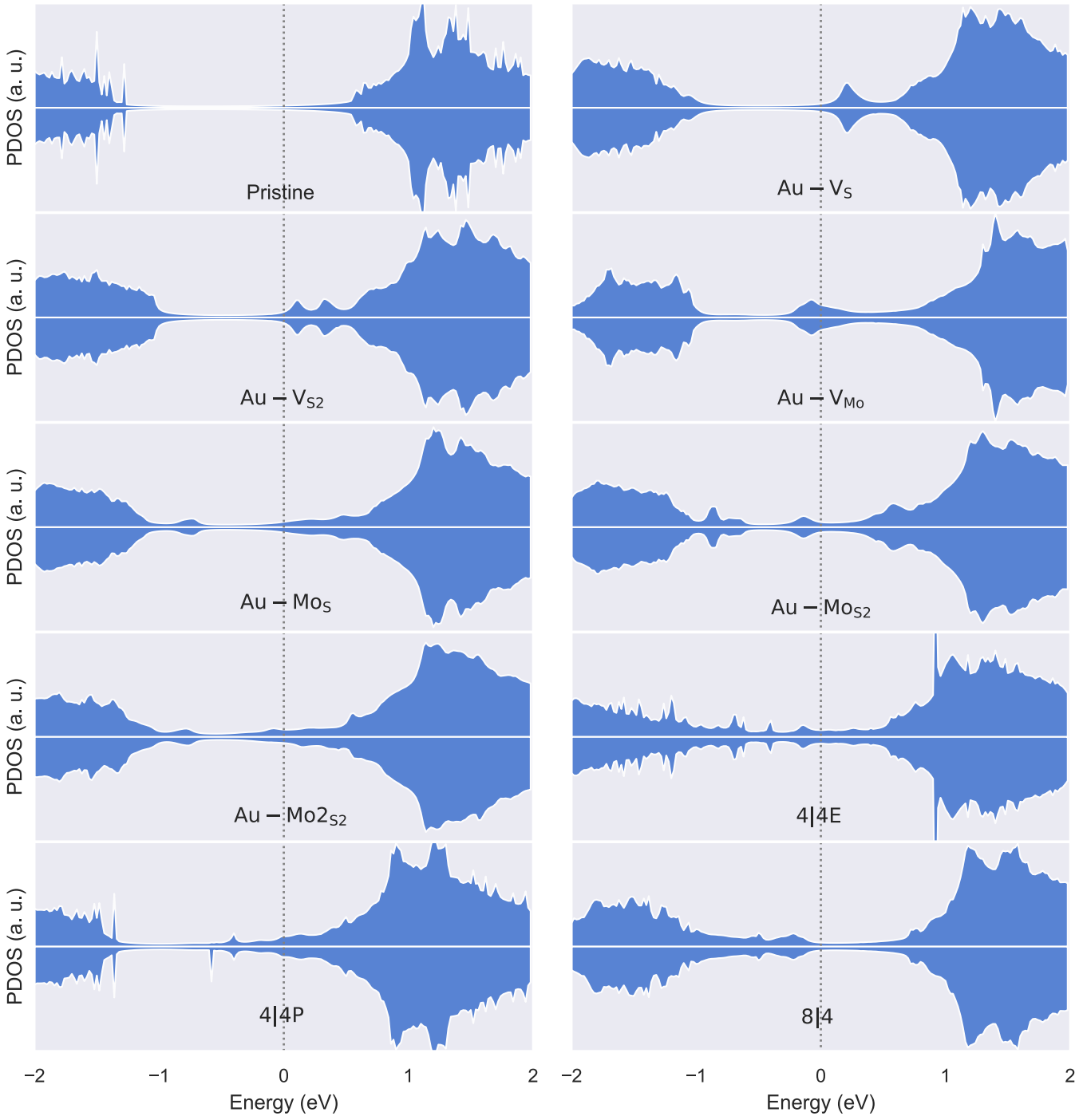

Figure 8: Projected density of states (PDOS) obtained from the Green's function surface simulations of Au-MoS_2 interfaces with the inclusion of grain boundaries, centered around the Fermi level of each system. The projections are onto the 4d orbitals of the core Mo atoms of MoS_2.

at ∼-0.7 eV in the spin down channel to be due to some numerical error in the adopted DOS integration scheme.

4 Conclusions

To conclude, we used density functional theory simulations to extensively investigate the impact of both point and extended defects on the properties of MoS_2 in contact with the Au electrode. To accurately simulate realistic Au-MoS_2 interfaces we employed a surface model based on the Green's function formalism. We chose to focus mainly on the most abundant defects with either CVD (that is, V_S, V_{S2}, V_{Mo}) or PVD (i.e., Mo_S, Mo_{S2}, $Mo2_{S2}$) growth processes. Among the grain boundaries, we modelled three representative cases characterized by a tilt angle of 60° (4|4P, 4|4E, 8|4). See Figure 2 and Figure 4 for the optimized geometries of point defect and grain boundary structures, respectively.

First, in order to decouple the effect of the Au electrode from that of defects in MoS_2, we investigated the impact of small point defects and grain boundaries on the electronic properties of free-standing single-layer MoS_2. We found that each point defect caused the appearance of a number of extra states in the original material's band gap, as can be seen in Figure 3. For instance S mono- and di-vacancies led to extra gap states located above the Fermi level and near the conduction band edge of the material, whereas one single Mo vacancy introduced a higher number of deep mid-gap states both above and below the Fermi level of MoS_2. Similarly, we observed that also antisite Mo defects introduced intra-gap states and caused a non-zero spin magnetic moment in the material. Finally, we could observe that grain boundaries 4|4P and 4|4E behave as "metallic-like strips" in MoS_2 by leading to the formation of a high number of intra-gap states extending throughout the whole original material's band gap. Contrary to such a behavior, we found 8|4 to cause extra mid-gap states located above the Fermi level of the material. Therefore, it is evident that defects have a non-negligible effect on the electronic properties of MoS_2.

In the second and main part of this work we constructed interfaces between both pristine and defective MoS_2 and the Au(111) electrode. More specifically, we explored: i) how the structure of both materials changed upon the formation of the contact; ii) the impact of defects on the orbital overlap and the metal-to-MoS_2 tunnelling probability; iii) how the electronic properties of defected MoS_2 are affected by the presence of the metal electrode.

We started to model the defect-free interface, and we found that the contact between Au and MoS_2 is characterized by weak dispersion interactions, i.e., a van der Waals gap. From the structural point of view, we could corroborate this by the large interface separation distance (2.71 Å) between the materials (see Figure 5), and by computing the electron density difference (EDD) map of the whole system upon the formation of the contact, shown in Figure 6. Indeed, the EDD map showed that there is some limited charge redistribution mainly at the MoS_2 surface. In general, a weak vdW gap would correlate with a low electron injection rate and with a limited effect on the electronic properties of the 2D material. Our simulations confirmed such an hypothesis, as we found a low tunnelling barrier of 19.4% (shown in Table 2) and no metallization of MoS_2 (see PDOS in Figure 8).

Then we started introducing defects in the material, and we found that S vacancies led to an overall small decrease of the quality of the metal contact. On average, the interface distance between Au and MoS_2 did not change but we could observe some degree of disorder in the bottom-most Au layer, leading to a limited atomic rearrangement in the metal. Electron injection rates from the metal to the 2D material were found to slightly decrease with respect to the pristine case to 18.5-18.3%, and once again we could not observe the significant formation of interfacial gap states. Interestingly, increasing the concentration of S vacancies up to $10^{14}\,cm^{-2}$ further decreased the tunnelling probability up to 18.0%. On the other hand, the Mo single vacancy significantly improved the quality of the contact, as we could see by the relaxed interface geometry and the EDD map, which shows a significant charge redistribution in both MoS_2 and the Au electrode. Moreover, the tunnelling probability dramatically increased to 64.1%, confirming the higher level of hybridization between the Au 5d orbitals and the 3p and 4d orbitals of S and Mo, respectively. Such an hybridization can be also observed in the PDOS of the system in Figure 8. As the PDOS crosses the Fermi level, we can also note the metallization of MoS_2.

In the case of antisite Mo defects, we observed an overall improvement of the Au-MoS_2 contact, and our results suggest this to be due to the presence of the extra Mo atom acting as a conductive bridge between the electrode and the 2D material. EDD maps corroborate this, as a large charge redistribution can be observed on the antisite Mo. Indeed, we found this to correlate with an improved electron injection rate, which increased above ∼25% for each of the three antisite Mo systems here considered. Also, the presence of interfacial gap states in the MoS_2 PDOS was evident.

The presence of grain boundaries led to a shorter interface separation between Au and the 2D material. This should correlate with a better electron injection rate and a strongerAu-MoS_2 interaction. Indeed, this was later confirmed by our further simulations: tunnelling probabilities increased up to 27.3%, and once again the increased orbital overlap was evident by looking at the formation of interfacial gap states in the PDOS plot of each system.

In conclusion, our results showed that defects have a significant impact on the Au-MoS_2 contact properties by either worsening or improving the quality of the MoS_2-metal interface. Interestingly, we point out that S vacancies, which have a detrimental effect, are generated mainly via CVD, whereas Mo antisite defects, which instead improve the contact, mainly with PVD. This shows how crucial the MoS_2 growth method is, as it does not only influence the material itself but also the properties at the metal contact. Based on our results, we could argue that, from the point of view of the quality of the metal contact, PVD-MoS_2 should lead to a decrease in the contact resistance. This should be beneficial in devices like 2D-FETs to reduce the power consumption and to improve the performance. On the contrary, CVD-MoS_2 might be preferred in devices like memristors based on single-layer MoS_2, as S vacancies appear to have a central role in the device working mechanism. Mo single vacancies, which dramatically improve the electron injection rate, are also mainly

generated via CVD, however the typical Mo defect density is orders of magnitude lower than that of S mono-vacancies. Here, defect engineering might be a viable solution to increase the concentration of such a vacancy to improve the contact. The grain boundaries considered in this work were all shown to reduce the average interface distance, and therefore if the aim is to increase the metal-to-MoS_2 tunnelling probability, the engineering of the grain boundaries could also be a viable option to increase the concentration of such extended defects.

Clearly, it is worth noting that in real devices other factors may further complicate the quality of the metal-MoS_2 interaction. For instance, it is highly likely that more than a single type of defect is present in the material. Similarly, defects and grain boundaries are likely to coexist in MoS_2. Extra adatoms deriving either from the growth or the transfer processes may also be present. Nevertheless, we expect our study to provide guidance on how to design metal contacts depending on the device application, and to which growth technique may be best suited for the purpose.

Acknowledgement

The authors ackowledge funding from the European Union's Horizon 2020 research and innovation programme, EU H2020 NeurONN project (www.neuronn.eu), grant agreement No. 871501. This work was granted access to the HPC/AI resources of CINES (Centre Informatique National de l'Enseignement Supérieur) under the allocation 2020-A0090811060 made by GENCI (Grand Équipement National de Calcul Intensif).

References

[1] D. Akinwande, N. Petrone, and J. Hone. Two-dimensional flexible nanoelectronics. *Nat. Commun.*, 5:5678, 2014.

[2] S. Lee and Z. Zhong. Nanoelectronic circuits based on two-dimensional atomic layer crystals. *Nanoscale*, 6:13283–13300, 2014.

[3] M. Dragoman, A. Dinescu, and D. Dragoman. 2d materials nanoelectronics: New concepts, fabrication, characterization from microwaves up to optical spectrum. *Phys. Status Solidi A*, 216:1800724, 2019.

[4] X. Jing, Y. Illarionov, E. Yalon, P. Zhou, T. Grasser, Y. Shi, and M. Lanza. Engineering field effect transistors with 2d semiconducting channels: Status and prospects. *Adv. Funct. Mater.*, 30:1901971, 2020.

[5] Y. Y. Illarionov, T. Knobloch, M. Jech, M. Lanza, D. Akinwande, M. I. Vexler, T. Mueller, M. C. Lemme, G. Fiori, F. Schwierz, and T. Grasser. Insulators for 2d nanoelectronics: the gap to bridge. *Nat. Commun.*, 11:3385, 2020.

[6] B. Radisavljevic, A. Radenovic, J. Brivio, V. Giacometti, and A. Kis. Single-layer MoS_2 transistors. *Nat. Nanotechnol.*, 6:147–150, 2011.

[7] S. Ahmed and J. Yi. Two-dimensional transition metal dichalcogenides and their charge carrier mobilities in field-effect transistors. *Nano-Micro Lett.*, 9:50, 2017.

[8] K. F. Mak, C. Lee, J. Hone, J. Shan, and T. F. Heinz. Atomically thin MoS_2: A new direct-gap semiconductor. *Phys. Rev. Lett.*, 105:136805, 2010.

[9] D. Lembke and A. Kis. Breakdown of high-performance monolayer MoS_2 transistors. *ACS Nano*, 6:10070–10075, 2012.

[10] A. Nourbakhsh, A. Zubair, R. N. Sajjad, A. K. G. Tavakkoli, W. Chen, S. Fang, X. Ling, J. Kong, M. S. Dresselhaus, E. Kaxiras, K. K. Berggren, D. Antoniadis, and T. Palacios. MoS_2 field-effect transistor with sub-10 nm channel length. *Nano Lett.*, 16:7798–7806, 2016.

[11] R. Ge, X. Wu, M. Kim, J. Shi, S. Sonde, L. Tao, Y. Zhang, J. C. Lee, and D. Akinwande. Atomristor: Nonvolatile resistance switching in atomic sheets of transition metal dichalcogenides. *Nano Lett.*, 18:434–441, 2018.

[12] S. Bhattacharjee, E. Caruso, N. McEvoy, C. Ó Coileáin, K. O'Neill, L. Ansari, G. S. Duesberg, R. Nagle, K. Cherkaoui, F. Gity, and P. K. Hurley. Insights into multilevel resistive switching in monolayer MoS_2. *ACS Appl. Mater. Interfaces*, 12:6022–6029, 2020.

[13] T. Carey, A. Arbab, L. Anzi, H. Bristow, F. Hui, S. Bohm, G. Wyatt-Moon, A. Flewitt, A. Wadsworth, N. Gasparini, J. M. Kim, M. Lanza, I. McCulloch, R. Sordan, and F. Torrisi. Inkjet printed circuits with 2d semiconductor inks for high-performance electronics. *Adv. Electron. Mater.*, 7:2100112, 2021.

[14] J. Hong, Z. Hu, M. Probert, K. Li, D. Lv, X. Yang, L. Gu, N. Mao, Q. Feng, L. Xie, J. Zhang, D. Wu, Z. Zhang, C. Jin, W. Ji, X. Zhang, J. Yuan, and Z. Zhang. Exploring atomic defects in molybdenum disulphide monolayers. *Nat. Commun.*, 6:6293, 2015.

[15] R. Addou, L. Colombo, and R. M. Wallace. Surface defects on natural MoS_2. *ACS Appl. Mater. Interfaces*, 7:11921–11929, 2015.

[16] S. Wang, G.-D. Lee, S. Lee, E. Yoon, and J. H. Warner. Detailed atomic reconstruction of extended line defects in monolayer MoS_2. *ACS Nano*, 10:5419–5430, 2016.

[17] S. Bertolazzi, S. Bonacchi, G. Nan, A. Pershin, D. Beljonne, and P. Samorì. Engineering chemically active defects in monolayer MoS_2 transistors via ion-beam irradiation and their healing via vapor deposition of alkanethiols. *Adv. Mater.*, 29:1606760, 2017.

[18] Y. Chen, S. Huang, X. Ji, K. Adepalli, K. Yin, X. Ling, X. Wang, J. Xue, M. Dresselhaus, J. Kong, and B. Yiildiz. Tuning electronic structure of single layer MoS_2 through defect and interface engineering. *ACS Nano*, 12:2569–2579, 2018.

[19] A. Mahata, J.-W. Jiang, D. R. Mahapatra, and T. Rabczuk. Effect of intrinsic structural defects on mechanical properties of single layer MoS_2. *Nano-Struct. Nano-Objects*, 18:100247, 2019.

[20] H. Schmidt, S. Wang, L. Chu, M. Toh, R. Kumar, W. Zhao, A. H. Castro Neto, J. Martin, S. Adam, B. Özyilmaz, and G. Eda. Transport properties of monolayer MoS_2 grown by chemical vapor deposition. *Nano Lett.*, 14:1909–1913, 2014.

[21] L. Li, R. Long, and O. Prezhdo. Why chemical vapor deposition grown MoS_2 samples outperform physical vapor deposition samples: Time-domain ab initio analysis. *Nano Lett.*, 18:4008–4014, 2018.

[22] M. Kim, R. Ge, X. Wu, X. Lan, J. Tice, J. C. Lee, and D. Akinwande. Zero-static power radio-frequency switches based on MoS_2 atomristors. *Nat. Commun.*, 9:2524, 2018.

[23] D. Li, B. Wu, X. Zhu, J. Wang, B. Ryu, W. D. Lu, W. Lu, and X. Liang. MoS_2 memristors exhibiting variable switching characteristics toward biorealistic synaptic emulation. *ACS Nano*, 12:9240–9252, 2018.

[24] X. Sun, Z. Wang, and Y. Q. Fu. Defect-mediated lithium adsorption and diffusion on monolayer molybdenum disulfide. *Sci. Rep.*, 5:18712, 2015.

[25] R. Xu, H. Jang, M.-H. Lee, D. Amanov, Y. Cho, H. Kim, S. Park, H.-J. Shin, and D. Ham. Vertical MoS_2 double-layer memristor with electrochemical metallization as an atomic-scale synapse with switching thresholds approaching 100 mv. *Nano Lett.*, 19:2411–2417, 2019.

[26] V. K. Sangwan, D. Jariwala, I. S. Kim, K.-S. Chen, T. J. Marks, L. J. Lauhon, and M. C. Hersam. Gate-tunable memristive phenomena mediated by grain boundaries in single-layer MoS_2. *Nat. Nanotechnol.*, 10:403–406, 2015.

[27] J. Kang, W. Liu, D. Sarkar, D. Jena, and K. Banerjee. Computational study of metal contacts to monolayer transition-metal dichalcogenide semiconductors. *Phys. Rev. X*, 4:031005, 2014.

[28] H. Zhong, R. Quhe, Y. Wang, Z. Ni, M. Ye, Z. Song, Y. Pan, J. Yang, M. Lei, J. Shi, and J. Lu. Interfacial properties of monolayer and bilayer MoS_2 contacts with metals: Beyond the energy band calculations. *Sci. Rep.*, 6:21786, 2016.

[29] K. Schauble, D. Zakhidov, E. Yalon, S. Deshmukh, R. W. Grady, K. A. Cooley, C. J. McClellan, S. Vaziri, D. Passarello, S. E. Mohney, M. F. Toney, A. K. Sood, A. Salleo, and E. Pop. Uncovering the effects of metal contacts on monolayer MoS_2. *ACS Nano*, 14:14798–14808, 2020.

[30] C. Gong, L. Colombo, R. M. Wallace, and K. Cho. The unusual mechanism of partial fermi level pinning at metal-MoS_2 interfaces. *Nano Lett.*, 14:1714–1720, 2014.

[31] A. Allain, J. Kang, K. Banerjee, and A. Kis. Electrical contacts to two-dimensional semiconductors. *Nat. Mater.*, 14:1195–1205, 2015.

[32] Y. Xu, C. Cheng, S. Du, J. Yang, B. Yu, J. Luo, W. Yin, E. Li, S. Dong, P. Ye, and X. Duan. Contacts between two- and three-dimensional materials: Ohmic, schottky, and p-n heterojunctions. *ACS Nano*, 10:4895–4919, 2016.

[33] S. S. Grønborg, S. Ulstrup, M. Bianchi, M. Dendzik, C. E. Sanders, J. V. Lauritsen, P. Hofmann, and J. A. Miwa. Synthesis of epitaxial single-layer MoS_2 on au(111). *Langmuir*, 31:9700–9706, 2015.

[34] F. Tumino, C. S. Casari, A. Li Bassi, and S. Tosoni. Nature of point defects in single-layer MoS_2 supported on au(111). *J. Phys. Chem. C*, 124:12424–12431, 2020.

[35] J. Yang, H. Kawai, C. P. Y. Wong, and K. E. J. Goh. Electrical doping effect of vacancies on monolayer MoS_2. *J. Phys. Chem. C*, 123:2933–2939, 2019.

[36] X. Qiu, Y. Wang, and Y. Jiang. First-principles study of vacancy defects at interfaces between monolayer MoS_2 and au. *RSC Adv.*, 10:28725, 2020.

[37] W. Zhou, X. Zou, S. Najmaei, Z. Liu, Y. Shi, J. Kong, J. Lou, P. M. Ajayan, B. I. Yakobson, and J.-C. Idrobo. Intrinsic structural defects in monolayer molybdenum disulfide. *Nano Lett.*, 13:52615–2622, 2013.

[38] J. Lin, S. T. Pantelides, and W. Zhou. Vacancy-induced formation and growth of inversion domains in transition-metal dichalcogenide monolayer. *ACS Nano*, 9:5189–5197, 2016.

[39] A. M. van der Zande, P. Y. Huang, D. A. Chenet, T. C. Berkelbach, Y. You, G. H. Lee, T. F. Heinz, D. R. Reichman, D. A. Muller, and J. C. Hone. Grains and grain boundaries in highly crystalline monolayer molybdenum disulphide. *Nat. Mater.*, 12:554–561, 2013.

[40] T. H. Ly, D. J. Perello, J. Zhao, Q. Deng, H. Kim, G. H. Han, S. H. Chae, H. Y. Jeong, and Y. H. Lee. Misorientation-angle-dependent electrical transport across molybdenum disulfide grain boundaries. *Nat. Commun.*, 7:10426, 2016.

[41] H.-P. Komsa and A. V. Krasheninnikov. Engineering the electronic properties of two-dimensional transition metal dichalcogenides by introducing mirror twin boundaries. *Adv. Electron. Mater.*, 3:1600468, 2017.

[42] X. Qiu, Y. Wang, and Y. Jiang. Dopants and grain boundary effects in monolayer MoS_2: A first-principles study. *Phys. Chem. Chem. Phys.*, 23:11937–11943, 2021.

[43] X. Zou and B. I. Yakobson. An open canvas-2d materials with defects, disorder, and functionality. *Acc. Chem. Res.*, 48:73–80, 2015.

[44] N. Gao, Y. Guo, S. Zhou, Y. Bai, and J. Zhao. Structures and magnetic properties of MoS_2 grain boundaries with antisite defects. *J. Phys. Chem. C*, 121:12261–12269, 2017.

[45] P. Johari and V. B. Shenoy. Tuning the electronic properties of semiconducting transition metal dichalcogenides by applying mechanical strains. *ACS Nano*, 6:5449–5456, 2012.

[46] N. Wakabayashi, H. G. Smith, and R. M. Nicklow. Lattice dynamics of hexagonal MoS_2 studied by neutron scattering. *Phys. Rev. B*, 12:659, 1975.

[47] S. Smidstrup, T. Markussen, P. Vancraeyveld, J. Wellendorff, J. Schneider, T. Gunst, B. Verstichel, D. Stradi, P. A. Khomyakov, U. G. Vej-Hansen, et al. Quantumatk: An integrated platform of electronic and atomic-scale modelling tools. *J. Phys: Condens. Matter*, 32:015901, 2020.

[48] QuantumATK version S-2021.06, Synopsys QuantumATK (www.synopsys.com/silicon/quantumatk.html).

[49] J. P. Perdew, K. Burke, and M. Ernzerhof. Generalized gradient approximation made simple. *Phys. Rev. Lett.*, 77:3865–3868, 1996.

[50] M. J. van Setten, M. Giantomassi, E. Bousquet, M. J. Verstraete, D. R. Hamann, X. Gonze, and G.-M. Rignanese. The pseudodojo: Training and grading a 85 element optimized norm-conserving pseudopotential table. *Comput. Phys. Commun.*, 226:39–54, 2018.

[51] Stefan Grimme. Semiempirical gga-type density functional constructed with a long-range dispersion correction. *J. Comput. Chem.*, 27(15):1787–1799, 2006.

[52] H. J. Monkhorst and J. D. Pack. Special points for brillouin-zone integrations. *Phys. Rev. B*, 13:5188–5192, 1976.

[53] S. Smidstrup, D. Stradi, J. Wellendorff, P. A. Khomyakov, U. G. Vej-Hansen, M.-E. Lee, T. Ghosh, E. Jónsson, H. Jónsson, and K. Stokbro. First-principiuples green's-function method for surface calculations: A pseudopotential localized basis set approach. *Phys. Rev. B*, 96:195309, 2017.

[54] D. Wang, W. Ju, T. Li, Q. Zhou, Z. Gao, and Y. Zhang. Electronic and magnetic properties of MoS_2 monolayers with antisite defects. *J. Phys. Chem. Solids*, 131:119–124, 2019.

[55] M. Gibertini and N. Marzari. Emergence of one-dimensional wires of free carriers in transition-metal-dichalcogenide nanostructures. *Nano Lett.*, 15:6229–6238, 2015.

[56] I. Popov, G. Seifert, and D. Tománek. Designing electrical contacts to MoS_2 monolayers: A computational study. *Phys. Rev. Lett.*, 108:156802, 2012.

[57] J. Zheng, Y. Wang, L. Wang, R. Quhe, Z. Ni, W.-N. Mei, Z. Gao, D. Yu, J. Shi, and J. Lu. Interfacial properties of bilayer and trilayer graphene on metal substrates. *Sci. Rep.*, 3:2081, 2013.

[58] Q. Wang, B. Deng, and X. Shi. A new insight for ohmic contacts to MoS_2: by tuning MoS_2 affinity energies but not metal work-functions. *Phys. Chem. Chem. Phys.*, 19:26151, 2017.

[59] N. Kaushik, A. Nipane, F. Basheer, S. Dubey, S. Grover, M. M. Deshmukh, and S. Lodha. Schottky barrier heights for au and pd contacts to MoS_2. *Appl. Phys. Lett.*, 105:113505, 2014.

[60] C. Kim, I. Moon, D. Lee, M. S. Choi, F. Ahmed, S. Nam, Y. Cho, H.-J. Shin, S. Park, and W. J. Yoo. Fermi level pinning at electrical metal contacts of monolayer molybdenum dichalcogenides. *ACS Nano*, 11:1588–1596, 2017.

[61] H. Lee, S. Deshmukh, J. Wen, V. Z. Costa, J. S. Schuder, M. Sanchez, A. S. Ichimura, E. Pop, B. Wang, and A. K. M. Newaz. Layer-dependent interfacial transport and optoelectrical properties of MoS_2 on ultraflat metals. *ACS Appl. Mater. Interfaces*, 11:31543–31550, 2019.

[62] Z. He, R. Zhao, X. Chen, H. Chen, Y. Zhu, H. Su, S. Huang, J. Xue, J. Dai, S. Cheng, M. Liu, X. Wang, and Y. Chen. Defect engineering in single-layer MoS_2 using heavy ion irradiation. *ACS Appl. Mater. Interfaces*, 10:42524–42533, 2018.

[63] W.-J. Xie, X. Li, and F.-J. Zhang. Mo-vacancy induced high performance for photocatalytic hydrogen production over MoS_2 nanosheets cocatalyst. *Chem. Phys. Lett.*, 746:137276, 2020.

[64] Y. He, P. Tang, Z. Hu, Q. He, C. Zhu, L. Wang, Q. Zeng, P. Golani, G. Gao, W. Fu, Z. Huang, C. Gao, J. Xia, X. Wang, X. Wang, C. Zhu, Q. R. Ramasse, A. Zhang, B. An, Y. Zhang, S. Martí-Sánchez, J. R. Morante, L. Wang, B. K. Tay, B. I. Yakobson, A. Trampert, H. Zhang, M. Wu, Q. J. Wang, J. Arbiol, and Z. Liu. Engineering grain boundaries at the 2d limit for the hydrogen evolution reaction. *Nat. Commun.*, 11:57, 2020.

[65] P. Man, D. Srolovitz, J. Zhao, and T. H. Ly. Functional grain boundaries in two-dimensional transition-metal dichalcogenides. *Acc. Chem. Res.*, 54:4191–4202, 2021.

[66] X. Wang, B. Wang, Q. Zhang, Y. Sun, E. Wang, H. Luo, Y. Wu, L. Gu, H. Li, and K. Liu. Grain-boundary engineering of monolayer MoS_2 for energy-efficient lateral synaptic devices. *Adv. Mater.*, 33:2102435, 2021.

[67] M. Fontana, T. Deppe, A. K. Boyd, M. Rinzan, Liu A. Y., M. Paranjape, and P. Barbara. Electron-hole transport and photovoltaic effect in gated MoS_2 schottky junctions. *Sci. Rep.*, 3:1634, 2013.